PAPER

Check for updates

Highly efficient core–shell Ag@carbon dot modified TiO$_2$ nanofibers for photocatalytic degradation of organic pollutants and their SERS monitoring†

Jing Jin, Wei Song, [iD] * Ning Zhang, Linjia Li, Hao Liu, Bai Yang [iD] and Bing Zhao [iD] *

In the present study, a novel hybrid nanomaterial composed of core–shell structured Ag@carbon dot (CD) modified TiO$_2$ nanofibers (NFs) was successfully fabricated *via* a simple two-step strategy for the first time. Herein, the Ag@CDs–TiO$_2$ NFs are demonstrated to be an efficient SERS substrate. The strong LSPR-induced electromagnetic enhancement (EM) by Ag@CDs NPs and efficient charge transfer (CT) effect between Ag@CDs and TiO$_2$ NFs synergistically contribute to the excellent SERS enhancement. In addition, the Ag@CDs–TiO$_2$ NFs exhibit enhanced photocatalytic activity regarding the organic pollutant degradation under visible light irradiation because of the enhanced light absorption and improved separation of photo-generated electron–hole pairs. Thus, this new nanocomposite can be used as a sensitive SERS substrate for determining the catalytic activity and reaction kinetics during the photodegradation of methylene blue (MB). Compared with UV-vis spectroscopy, the SERS technique enables more accurate monitoring of the changes of adsorption molecules and actual catalytic process on the surface of the catalyst. These results are significant for the development of metal or semiconductor-based catalysts for ensuring optoelectronic, energy and environmental applications.

Introduction

Surface-enhanced Raman Scattering (SERS) is the phenomenon that Raman signals are significantly improved resulting from the electromagnetic (EM) enhancement on rough metal or other nanomaterial surface substrates and the efficient charge transfer (CT) effect between the substrates and the adsorbed molecules.[1–5] It has shown a large variety of promising applications in sensing, catalysis, environmental monitoring, and medical diagnosis.[6–8] Recently, heterogeneous catalytic reaction has attracted dramatic attention and extensive research interest. Many great efforts have also been made in the investigation of the mechanism of the heterogeneous reaction; some spectroscopic techniques including UV-vis absorption spectroscopy, infrared and Raman techniques have been widely used, however, usually displaying the disadvantages of low sensitivity. Compared with above-mentioned techniques, SERS exhibits the advantages of high sensitivity, nondestructive and *in situ* detection, which enables one to monitor accurately the changes of adsorption molecules and actual catalytic process on the surface of the catalyst.[9–12] Therefore, it is a great significance

to construct a novel multifunctional materials with both efficient SERS property and catalytic activity to monitor the catalytic process and study the mechanism of the catalytic reaction.

Titanium dioxide (TiO$_2$) is one of the most prominent semiconductor photocatalysts with superior optoelectronic properties.[13–15] Under the light irradiation with $h\nu \geq E_g$ (band gap), the TiO$_2$ absorbs photons and produces electron–hole pairs. The photon-induced holes have an outstanding ability to capture electrons to show strong oxidation, which can activate and oxidize organic materials. However, TiO$_2$ possesses large bandgap of about 3.2 eV and only absorb the light in the near ultraviolet (UV) region (wavelength < 400 nm), which restricts visible light harvesting and charge collection, then decreases the visible photocatalytic activity. Localized surface plasmon resonance (LSPR) effect have been demonstrated for broad utilization in the fields of photocatalysis, solar cells and photovoltaics device due to the efficient light harvesting capability. LSPR is a collective oscillation of conduction band electrons in metal nanoparticles (NPs) driven by the electromagnetic field of incident light, which could significantly increase the light absorption and the generation of the photon-carriers. During past years, plasmonic noble metal NPs such as Au, Ag, Pd have been reported to be combined with TiO$_2$ to improve light-harvesting, reducing the possibility of electron–hole recombination and then enhancing the efficiency of photocatalytic reactions.[16–21] Currently, the photocatalytic

State Key Laboratory of Supramolecular Structure and Materials, Jilin University, Changchun 130012, P. R. China. E-mail: weisong@jlu.edu.cn; zhaob@jlu.edu.cn

properties of carbon dots (CDs) have attracted broad attention because they have a wide light absorption range and can accelerate the separation efficiency of photo-generated charge carriers.[22] In particular, the light-harvesting ability and charge separation transfer dynamics can be significantly improved by coupling CDs with TiO_2.[23–27] Based on the above analysis, it is a meaningful strategy to accelerate the photocatalytic efficiency by the combination of TiO_2 with both noble metal NPs and CDs, which can not only improve the light absorption range but also enhance the charge separation ability.

In the present study, a novel hybrid nanomaterial composed of core–shell structured Ag@CDs modified TiO_2 (Ag@CDs–TiO_2) nanofibers (NFs) was successfully fabricated via a simple two-step strategy. Herein, the Ag@CDs–TiO_2 NFs were demonstrated to be as efficient SERS substrates. The strong interactions between TiO_2 NFs and Ag@CDs afford continuous delocalized surface plasmons and efficiently interfacial charge separation, generating a large electromagnetic (EM) field enhancement and efficient CT ability, contributing to the excellent SERS enhancement. In addition, the Ag@CDs–TiO_2 hybrid NFs exhibit superior photocatalytic activity regarding the organic pollutants degradation under visible light irradiation owing to their enhanced light absorption ability and improved separation of photo-generated electron–hole pairs. Thus, the new Ag@CDs–TiO_2 hybrid NFs can be used as a sensitive SERS substrate for determining the catalytic efficiency and reaction kinetics towards the photodegradation of methylene blue (MB). These results are significant for the development of metal or semiconductor-based catalysts for ensuring optoelectronic, energy and environmental applications.

Experimental

Materials and methods

$AgNO_3$ was bought from Sinopharm Chemical Reagent Co., Ltd. NaOH, $NaBH_4$, sodium citrate, citric acid, ethylenediamine, MB were purchased from Beijing Chemical Works. Poly(vinylpyrrolidone) (PVP) (M_W = 1 300 000 g mol^{-1}) and p-thiophenol (PATP) were obtained from Sigma-Aldrich. Tetrabutyl titanate was obtained from the Guangfu Chem. Co. (China). CDs and TiO_2 NFs were prepared with the similar procedures based on the previous reports.[28,29]

Fabrication of Ag@CDs–TiO_2 hybrid NFs

The procedure for the fabrication of the Ag@CDs–TiO_2 hybrid NFs is as follows: TiO_2 NFs and $AgNO_3$ aqueous solution were mixed under stirring for 30 min, then CDs and NaOH were added to form a mixed aqueous solution containing of TiO_2 NFs (0.006 mg mL^{-1}), CDs (33 mg mL^{-1}), $AgNO_3$ (0.2 mmol L^{-1}) and NaOH (0.01 mol L^{-1}). After that, the mixing solution was heated at 50 °C for 5 min until a stable dark brown suspension was produced. Then the suspension was centrifuged and washed with water for twice. The sample was re-dispersed in 6 mL of deionized water for further use. In addition, the prepared Ag@CDs–TiO_2 hybrid can be regarded as the TiO_2 NFs as a hard template to in situ grow core–shell structured Ag@CDs NPs on

their surface. Core–shell structured Ag@CDs NPs with a similar size (25 nm) of the Ag@CDs on the surface of TiO_2 NFs were prepared through the direct reduction of $AgNO_3$ by CDs based on our previous reports.[12] As shown in Fig. S1b,† the HRTEM image also displays the core–shell structured Ag@CDs with the average sizes of 25 nm. In addition, the controlled sample of TiO_2–Ag was prepared by mixing TiO_2 NFs with $AgNO_3$ solution using sodium citrate as reducing agent. And TiO_2–CDs have also been prepared by heating the aqueous mixture of TiO_2 NFs and CDs at 50 °C.

Preparation of individual Ag NPs by $NaBH_4$ and sodium citrate

Ag NPs with an average diameter of ca. 25 nm was prepared by stepwise seeded growth method. Firstly, citrate-capped 4 nm Ag NPs was synthesized with citrate solution and $NaBH_4$ based on the previous report.[30] And then one-step seeded growth of Ag NPs was carried out with the Lee–Meisel method. Typically, 2 mL of 1% citrate solution was mixed with 80 mL of water in 250 mL three-necked round bottom flasks equipped with a reflux condenser, and brought to boiling. Next, 8 mL of starter seeds solution was added into the above solution under vigorously stirring, followed by the addition of 1.7 mL of 1% $AgNO_3$ solution. After 1 h reaction and cooling down to room temperature, as shown in Fig. S1a,† the HRTEM image shows that the average sizes of Ag NPs is 25 nm.

SERS measurement

In a typical experiment, PATP were used as Raman probes to estimate SERS activity of Ag@CDs–TiO_2 hybrid. For the SERS measurement, Ag@CDs–TiO_2 hybrid was mixed with PATP solution with final different concentrations from 10^{-10} to 10^{-4} M for 1 h, then the mixed solution was centrifuged and washed for three times to remove the excess PATP molecules. The above solution of PATP molecules with different concentrations adsorbed on the surface of Ag@CDs–TiO_2 hybrid was transferred for Raman measurements under a continuous 532 nm laser excitation.

Catalytic measurement

The photocatalytic degradation of MB was carried out in a culture dish containing 10^{-5} M MB and CDs, TiO_2 NFs, Ag NPs, Ag@CDs and Ag@CDs–TiO_2 hybrid NFs as catalysts with the same concentrations, respectively. First, the mixture was stirred in the dark for 30 min to achieve adsorption–desorption equilibrium. Then, the reaction systems were conducted under visible light irradiation by using a 300 W Xe lamp with a 420–800 nm cut-off filter under the same conditions. The reaction progress was monitored at a regular time interval of 4 min by the UV-vis spectra and SERS spectra under continuous 532 nm laser excitation.

Characterization

The morphologies of CDs, Ag NPs, TiO_2 NFs, Ag@CDs–TiO_2 hybrid NFs were characterized by the JEOL JEM-2100F transmission electron microscope (TEM) operated at 200 kV. UV-vis

spectra were obtained from Shimadzu UV-3600 UV-vis-NIR spectrophotometer. The fluorescence spectra were recorded on Shimadzu 5301PC fluorescence spectrometer. X-ray photo-electron spectroscopy (XPS) data were obtained from a Thermo ESCALAB 250 photoelectron spectrometer with Al Kα X-ray radiation. The catalytic measurement was obtained from a Xe lamp (CEL-HXF300, Beijing China Education Au-light Co., Ltd.). The Raman spectra were measured by Renishaw-1000 spectrometer with a He/Ne laser as excitation line of 532 nm, the laser power at the sample position was typically 1.1 mW. The spectrometer was calibrated by Raman band at 520.7 cm^{-1} of a Si wafer.

Results and discussion

Preparation, characterization and SERS properties of Ag@CDs–TiO$_2$ hybrid NFs

The general process for the construction of Ag@CDs–TiO$_2$ hybrid NFs is performed in Scheme 1. A one-pot *in situ* reduction reaction in an aqueous solution containing TiO$_2$, AgNO$_3$ and CDs was carried out to produce Ag@CDs–TiO$_2$ hybrid NFs at 50 °C. During the reduction reaction, Ag$^+$ was firstly adsorbed on the surface of TiO$_2$ NFs, then the CDs as the electron donor with abundant –OH and –NH$_2$ groups could directly reduce the Ag$^+$ to Ag NPs *via* electron transfer on the surface of TiO$_2$ NFs. Fig. 1a and b show typical TEM images of the prepared CDs, TiO$_2$ NFs. The diameters of the typical CDs are in the range of 2–6 nm, which is consistent with the previous report.[28] The diameter of TiO$_2$ NFs prepared by electrospinning is about 200 nm. Fig. 1c and d show the TEM and manifested HRTEM image of Ag@CDs–TiO$_2$ hybrid NFs respectively, it is clearly observed that the core–shell structured Ag@CDs consisting of Ag NPs cores with a mean diameter of *ca.* 25 nm and ultrathin continuous carbon shells with a thickness of *ca.* 2 nm are dispersed uniformly on the surface of TiO$_2$ NFs, and the inserted HRTEM image clearly demonstrates typical lattice spacings of 0.238 nm, which can be attributed to the (111) plane of face-centered cubic (fcc) metallic Ag.[12] The composition of the prepared Ag@CDs–TiO$_2$ hybrid NFs has also been confirmed by EDX mapping and spectrum, revealing the presence of Ag, Ti, C, O and Cu elements (Fig. 1e–i). The merged element mapping analysis demonstrates that the Ag NPs are uniformly coated on the surface of the TiO$_2$ NFs (Fig. 1e). The carbon element EDX mapping reveals that the background carbon are uniformly distributed on copper grid, however, the CDs carbon as a capping agent shows a larger density coated on
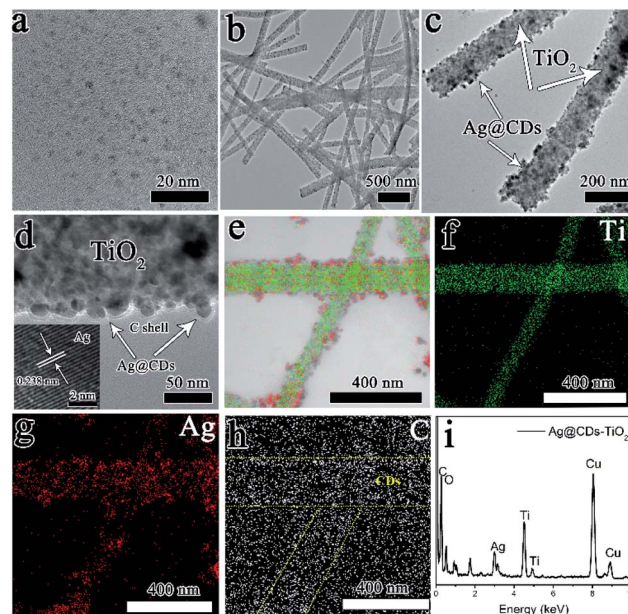

Fig. 1 TEM images of (a) CDs; (b) TiO$_2$ NFs; (c) Ag@CDs–TiO$_2$ hybrid NFs; (d) HRTEM image of Ag@CDs–TiO$_2$ hybrid NFs, inset: HRTEM image of Ag NPs with fringe spacing; (e) the merged mapping image of Ag@CDs–TiO$_2$ hybrid NFs and corresponding element mappings of (f) Ti; (g) Ag and (h) C; (i) EDX spectrum of the Ag@CDs–TiO$_2$ hybrid NFs.

the Ag NPs, demonstrating the existence of the CDs on the layer of Ag (the yellow highlighted parts are CDs). All of these results have confirmed the successful fabrication of Ag@CDs–TiO$_2$ hybrid NFs.

The electronic vibration and surface plasmon resonance formation of the Ag@CDs–TiO$_2$ hybrid NFs was characterized by UV-vis absorption spectroscopy. Fig. 2a demonstrates the UV-vis absorption spectrum of CDs aqueous solution with a yellow color, exhibiting an absorption peak at 340 nm, which is corresponding to the n–π* transition. The TiO$_2$ NFs shows a typical broad absorption at about 260–320 nm with the wide bandgap of about 3.2 eV, which is consistent with previous reports.[13] The prepared Ag@CDs–TiO$_2$ hybrid NFs exhibit a dark brown color and show a typical absorption band at 415 nm attributed to the LSPR absorption of Ag NPs. Moreover, it is observed that the Ag@CDs and Ag@CDs–TiO$_2$ NFs both exhibit red shift LSPR absorption peak compared with the individual Ag NPs with the same size, which can be due to an overall increasing in the refractive index of the dielectric environment surrounding the Ag NPs upon CDs coating and TiO$_2$ NFs. In addition, the Ag@CDs and Ag@CDs–TiO$_2$ also display enhanced and broaden plasmon absorption, which can be attributed to the unique structure and new construction of series new surface energy states (charge transfer (CT) complex: Ag-to-CDs CT transition) in Ag@CDs and Ag@CDs–TiO$_2$ because the CDs possess series independent energy levels. In this CT process, Ag NPs generate electrons driven by the surface plasmon excitation under light irradiation, then the electrons transfer from the Ag NPs to CDs. For Ag@CDs–TiO$_2$, it also involves an efficient CT effect among the Ag, CDs and TiO$_2$, which further enhance and
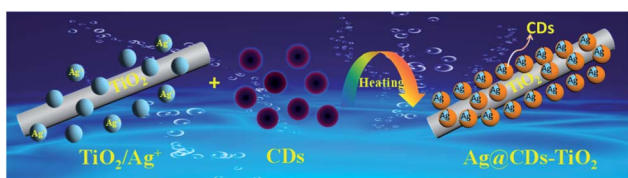
Scheme 1 Schematic illustration of the synthesis of Ag@CDs–TiO$_2$ hybrid NFs.
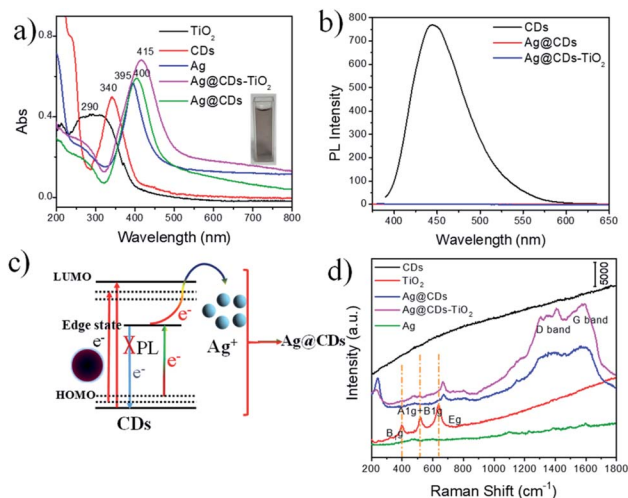
Fig. 2 (a) UV-vis absorption spectra of TiO$_2$ NFs, CDs, Ag NPs, Ag@CDs and Ag@CDs–TiO$_2$ hybrid NFs, inset: photographs of CDs and Ag@CDs–TiO$_2$ nanocomposites in aqueous solution under visible light; (b) typical PL excitation spectra of CDs, Ag@CDs and Ag@CDs–TiO$_2$ hybrid NFs in aqueous suspension; (c) mechanism of CDs PL quenching in Ag@CDs–TiO$_2$ hybrid NFs; (d) Raman spectra of CDs, TiO$_2$, Ag NPs, Ag@CDs and Ag@CDs–TiO$_2$ hybrid NFs in aqueous suspension.

broaden plasmon absorption. Furthermore, the Ag@CDs–TiO$_2$ hybrid NFs display an absorption extending into the visible light range, which are beneficial for their applications in the photocatalytic fields. It is well-known that CDs usually exhibit photoluminescence (PL) and excitation-dependent PL property. In our study, the CDs could emit strong blue luminescence under 370 nm (Fig. 2b) and excitation-dependent PL (Fig. S2†). However, the PL of CDs was quenched accompanied by the formation of Ag@CDs and Ag@CDs–TiO$_2$ hybrid NFs, which is resulting from an effective electron transfer process between CDs and Ag NPs in the synthesis process, contributing to the annihilation of the nonradiative electron/hole recombination in the CDs (Fig. 2c). The PL quenching of the CDs in the Ag@CDs–TiO$_2$ hybrid NFs is beneficial for studying their Raman and SERS properties. Fig. 2d shows the Raman spectrum of the TiO$_2$ NFs, CDs, Ag NPs, Ag@CDs and Ag@CDs–TiO$_2$ hybrid NFs. In TiO$_2$ NFs, three Raman peaks at 396, 518 and 640 cm^{-1} are assigned to the B$_{1g}$, A$_{1g}$ + B$_{1g}$ and E$_g$ modes, respectively. The Ag NPs have no typical Raman signal. The Raman spectrum of the CDs shows no obvious Raman signal because of the high fluorescence. However, the Raman spectrum of the Ag@CDs NPs exhibited obvious intrinsic peaks of carbon species at about 1350 (D band) and 1590 cm^{-1} (G band), which indicates that the formation of Ag@CDs NPs quenches the strong fluorescence of CDs and significantly allowed obvious Raman signals for CDs to be obtained. In Ag@CDs–TiO$_2$ hybrid NFs, the Raman peak attributed to TiO$_2$ NFs is unconspicuous, with the PL quenching of the system, the Raman intrinsic information of the D and G band of CDs at about 1350 and 1580 cm^{-1} can be also clearly observed. The XRD measurement has also been carried out to characterize the prepared Ag@CDs–TiO$_2$ hybrid NFs (Fig. S3†).

Compared with the TiO$_2$ nanofibers, the strong diffraction peaks at 38.1°, 44.3°, 64.5°, 77.5° are observed for Ag@CDs–TiO$_2$ hybrid NFs, which can be attributed to (111), (200), (220) and (311) planes of fcc structure of Ag, another strong diffraction peak at 33.7° and 55.5° can be ascribed to the formation of O=C–O–Ag, demonstrating the formation of Ag@CDs, which is similar with the previous report.[12]

The full-range XPS spectrum demonstrates the typical signals of C, O, N, Ti, and Ag elements for the Ag@CDs–TiO$_2$ hybrid NFs (Fig. 3a). In detail, as illustrated in Fig. 3b, the main peaks of C atoms in the Ag@CDs–TiO$_2$ hybrid NFs are observed at 284.4, 284.8, 285.2, 288.4 and 289.6 eV, which are attributed to C–C/C=C, C–N, C–O, C=O and COOH groups, respectively. In Fig. 3c, the main peaks of O 1s can be fitted with obvious peaks at 531.3, 532.0, 532.7 and 535.7 eV, which are assigned to Ti–O, C=O, C–O and N–O, respectively. For the N 1s fine spectrum in Fig. 3d, the peaks observed at 398.8, 399.5, 400.2 and 407.6 eV might be ascribed to pyridinic nitrogen, pyrrolic nitrogen, graphitic nitrogen and N–O groups, respectively.[31–33] In Fig. 3e, the Ag 3d peaks could be found with two doublet components; the low binding energy signals at 367.8 eV (Ag 3d$_{5/2}$) and 373.8 eV (Ag 3d$_{3/2}$) are associated with the metallic Ag.[34] For the Ti 2p spectrum in Fig. 3f, the peaks are observed at 458 eV (Ti 2p$_{3/2}$) and 464 eV (Ti 2p$_{1/2}$), which are in accordance with the reported value of the Ti^{4+} state in TiO$_2$.[35] This result is also consistent with the XPS spectrum of Ti in the prepared TiO$_2$ in Fig. S4,† demonstrating that TiO$_2$ has not changed after the formation of Ag@CDs–TiO$_2$ hybrid NFs. In a word, based on the XRD, XPS analysis and the TEM image of Ag@CDs–TiO$_2$, we can conclude that Ag NPs are dominated with metallic Ag, providing them good candidates for the SERS substrates.

Fig. 4a exhibits the SERS spectra of PATP probe molecules with different concentrations adsorbed on the surface of Ag@CDs–TiO$_2$ hybrid NFs. Several dominant main peaks of PATP are observed at 1077, 1144, 1390, 1435, and 1577 cm^{-1}, which are attributed to C–S stretching (7a, a$_1$), C–H bending (9b, b$_2$), C–H bending + C–C stretching (3b, b$_2$), C–H bending + C–C stretching (19b, b$_2$), and C–C stretching (8b, b$_2$), respectively. The SERS intensities of three characteristic peaks at 1390, 1435, and 1577 cm^{-1} decreased with the decreasing of PATP
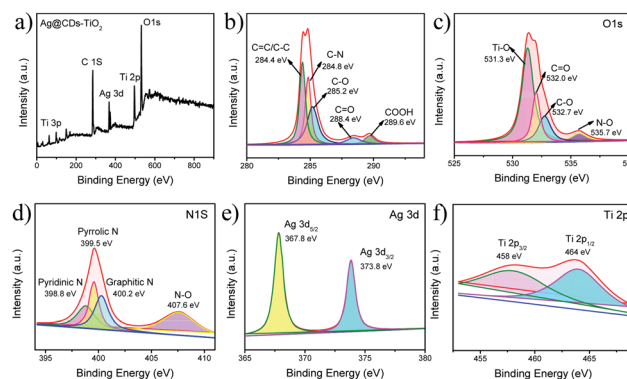

Fig. 3 XPS spectra of Ag@CDs–TiO$_2$ hybrid NFs: (a) full-range, (b) C 1s, (c) O 1s, (d) N 1s, (e) Ag 3d, (f) Ti 2p.
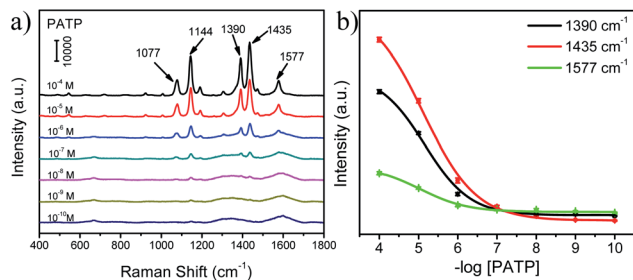
Fig. 4 (a) SERS spectra of PATP with different concentrations absorbed on Ag@CDs–TiO$_2$ hybrid NFs suspension. (b) SERS intensities at 1390, 1435, and 1577 cm^{-1} with different concentrations of PATP, where the error bar indicates three independent measurements.

Fig. 5 (a) Time-dependent absorbance spectra of the catalytic degradation of MB in the presence of Ag@CDs–TiO$_2$ hybrid NFs under visible light irradiation with different time. (b) UV-vis absorbance spectra of the catalytic degradation of MB in the presence of different kinds of photocatalysts (from top to bottom: blank MB unirradiated, blank MB, TiO$_2$ NFs, CDs, CDs–TiO$_2$, Ag NPs, Ag–TiO$_2$, Ag@CDs, and Ag@CDs–TiO$_2$ hybrid NFs) under visible light irradiation for 60 min. (c) Plots of $-\ln(C_t/C_0)$ versus time for rate constant calculation of the degradation of MB under visible light irradiation in the presence of different kinds of photocatalysts. (d) The SERS spectra of the catalytic degradation of MB under visible light irradiation in the presence of Ag@CDs–TiO$_2$ hybrid NFs. (e) The curve of relationship between the SERS intensity and the reaction time according to the bands at 1624 cm^{-1}. (f) The curve of the linear relationship between $-\ln(I_t/I_0)$ and the reaction time according to the bands at 1624 cm^{-1}.

concentrations (inset in Fig. 4a), and the peaks of the PATP molecules by using Ag@CDs–TiO$_2$ hybrid NFs as SERS substrate are similar to those of previous reports.[36] In addition, it is clearly observed that a PATP concentration as low as 10^{-9} M could be distinguishable. Furthermore, the enhancement factor (EF) was evaluated for the Ag@CDs–TiO$_2$ substrate, exhibiting a value of about 2.6×10^6, which is better or comparable with some typical Ag-based SERS substrates, indicating a high sensitivity of this substrate.[37–40] (EF calculation details are provided in the ESI.†) The unique SERS effect of Ag@CDs–TiO$_2$ hybrid NFs might be due to the superior CT effect between TiO$_2$, CDs and Ag NPs, the enhanced LSPR effect induced EM by Ag NPs and a homogeneous high density of "hot spots" caused by the uniform Ag@CDs–TiO$_2$ hybrid NFs. Hence, it can be supposed that the CT and EM coupling between the TiO$_2$, CDs and Ag components synergistically contribute to a high SERS activity.[41–44]

Visible photocatalytic activity of Ag@CDs–TiO$_2$ hybrid NFs

TiO$_2$ is a prominent semiconductor with excellent catalytic degradation ability under UV irradiation, the combination of TiO$_2$, noble metal and CDs can effectively improve the light absorption range and charge separation ability, then enhance the visible photocatalytic efficiency. Fig. 5a demonstrates the UV-vis spectrum of photocatalytic degradation of MB solution with the Ag@CDs–TiO$_2$ hybrid NFs under visible light irradiation, showing that the degradation process will complete in 60 min. We have also compared the photocatalytic activity of the prepared Ag@CDs–TiO$_2$ hybrid NFs with those of CDs, TiO$_2$ NFs, Ag NPs, Ag@CDs, TiO$_2$–Ag and TiO$_2$–CDs under visible light irradiation (Fig. 5b), and the peak absorbance *versus* various time is shown in Fig. 5c. It demonstrates that the prepared Ag@CDs–TiO$_2$ hybrid NFs show a much better photocatalytic activity than CDs, TiO$_2$ NFs, Ag NPs, Ag@CDs, TiO$_2$–Ag and TiO$_2$–CDs. The accelerated photocatalytic activity of the resultant Ag@CDs–TiO$_2$ hybrid NFs should be due to the improved light absorption range and charge separation ability under visible light irradiation.

Based on the above-mentioned results, Ag@CDs–TiO$_2$ hybrid NFs exhibit both excellent SERS properties and high photocatalytic performance; thus, we have used SERS spectroscopy to
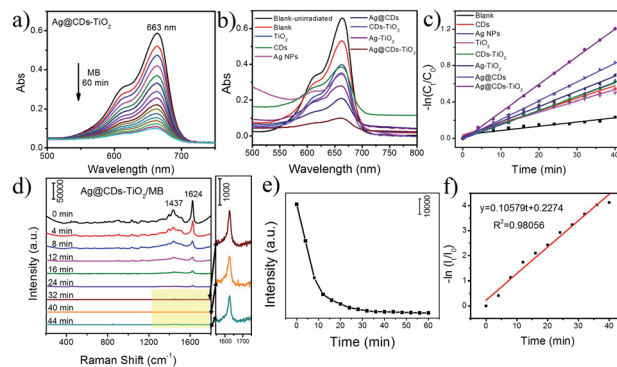
conduct the monitoring of MB degradation on the Ag@CDs–TiO$_2$ hybrid NFs under visible light irradiation. Fig. 5d demonstrates the SERS spectra of the catalytic degradation of MB under visible light irradiation in the presence of Ag@CDs–TiO$_2$ hybrid NFs. It is evident that the characteristic bands of MB appear before visible light irradiation; the characteristic bands at 1437 and 1624 cm^{-1} are attributed to N–H bending and C–C ring stretching modes, respectively.[18] During photocatalytic process under visible light irradiation, the Raman intensity of these MB bands gradually decreases with increasing time, and no other new peaks emerge, indicating the degradation of MB molecules. Compared the UV-vis absorption spectra with SERS spectra regarding the monitoring the photocatalytic process, it is found that the catalytic degradation reaction tends to equilibrium in 60 min in UV-vis absorption spectra, while in 40 min in SERS spectra (Fig. 5a and d). These results demonstrate that UV-vis absorption spectroscopy only reflects the photocatalytic reaction process in a solution, but not on the surface of a catalyst. However, SERS technique enables the monitoring accurately the changes of adsorption molecules and actual catalytic process on the surface of the catalyst. In order to reveal this phenomenon more clearly, the curve of the linear relationship between $\ln(I_t/I_0)$ and the reaction time according to the bands at 1624 cm^{-1} is provided in Fig. 5f. The reaction rate constant in SERS spectra is 0.10579, which is 3.54 times as high as that in UV-vis absorption spectra.

As aforementioned, the significantly enhanced photocatalytic activity of the Ag@CDs–TiO$_2$ hybrid NFs can be essentially attributed to the improved light absorption range

and charge separation ability. In this regard, a probable catalytic mechanism of Ag@CDs–TiO$_2$ hybrid NFs is illustrated in Scheme 2. One reason is that the CT process driven by the LSPR excitation. The LSPR excites electron–hole pairs in Ag NPs under visible light irradiation.[45–47] The CDs with unique photoelectric properties severing as excellent electronic acceptor to improve the efficient electron separation of the photo-induced hot electrons of Ag NPs to CDs and which in turn tends to get transferred into TiO$_2$. The remarkable CT ability of CDs and TiO$_2$ can suppress electron–hole recombination, which could be a promising strategy to improve the photocatalytic activity. Another reason is that CDs with unique quantum confinement effect and edge effect can provide series independent energy levels and band gaps, increasing the separation probability and efficiency of photo-generated electron–hole pairs in CDs under visible light irradiation, then the electrons in CDs can be transferred to the surface of TiO$_2$ and Ag NPs. In the photocatalytic reaction, the generating electron–hole pairs and their efficient CT ability improve the photocatalytic degradation of pollutants. Both mechanisms maybe exist in the photocatalytic reaction, the former of CT driven by LSPR excitation plays a dominant role, however, it is possible for the electron successfully transfer from the CDs to Ag, but the odds of the CDs trigger CT is very small because of the inadequate energy. It is well known that the photogenerated electrons are able to reduce O$_2$ to $\cdot$O$_2^-$ *via* an ultrafast one electron process and the holes can oxidize H$_2$O to produce $\cdot$OH, which can effectively degrade the dyes.[48] In a word, the LSPR effect of Ag NPs and the efficient electron transfer ability among Ag, CDs and TiO$_2$ increase light-harvesting and promote the electron–hole pairs generation and separation, all together contribute to the enhanced photocatalytic activity of Ag@CDs–TiO$_2$ hybrid NFs.
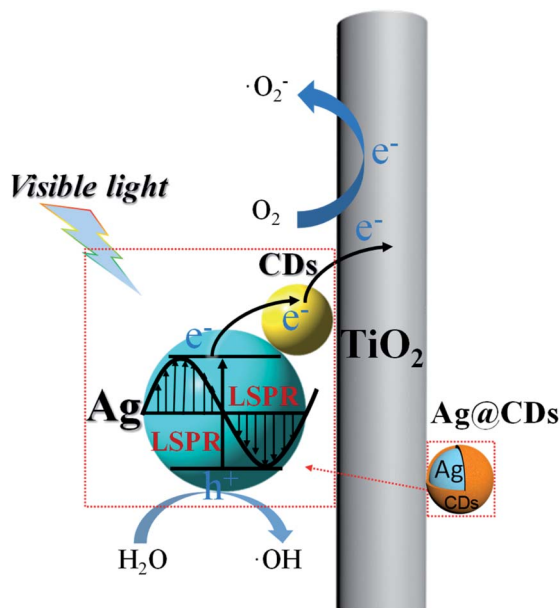
Scheme 2 The possible mechanism of enhanced photocatalytic performance of Ag@CDs–TiO$_2$ hybrid NFs.

Conclusions

In summary, we have successfully fabricated a novel hybrid nanomaterial composed of core–shell structured Ag@CDs modified TiO$_2$ nanofibers as both efficient SERS substrate and superior visible-light photocatalyst. The strong coupling of CT interactions between TiO$_2$ NFs, CDs, Ag NPs and LSPR-induced EM by Ag NPs synergistically contribute to the excellent SERS enhancement. In addition, the enhanced light absorption and improved separation of photo-generated electron–hole pairs lead to a superior photocatalytic performance under visible light irradiation. Consequently, this new nanocomposites has been successfully used as a sensitive SERS substrate for monitoring catalytic reactions, determining the catalytic activity and reaction kinetics of the photodegradation of organic pollutants. Compared with UV-vis absorption spectroscopy, SERS technique enables more accurately monitor the changes of adsorption molecules and actual catalytic process on the surface of the catalyst. The development of metal coupled with semiconductor-based SERS substrates or catalysts will provide great promise in catalysis, optoelectronic, energy and environmental applications.

Conflicts of interest

There are no conflicts to declare.

Acknowledgements

Notes and references

1 K. Kneipp, M. Moskovits and H. Kneipp, *Surface-Enhanced Raman Scattering: Physics And Applications*, Springer, Berlin, Germany, 2006.

2 Y. Ozaki, K. Kneipp and R. Aroca, *Single Nanoparticles and Single Cells*, Willey, United Kingdom, 2014.

3 J. F. Li, Y. F. Huang, Y. Ding, Z. L. Yang, S. B. Li, X. S. Zhou, F. R. Fan, W. Zhang, Z. Y. Zhou, D. Y. Wu, B. Ren, Z. L. Wang and Z. Q. Tian, *Nature*, 2010, **464**, 392–395.

4 W. Ji, L. Li, W. Song, X. Wang, B. Zhao and Y. Ozaki, *Angew. Chem., Int. Ed.*, 2019, **131**, 14591–14598.

5 J. H. Zhong, X. Jin, L. Y. Meng, X. Wang, H. S. Su, Z. L. Yang, C. T. Wiliams and B. Ren, *Nat. Nanotechnol.*, 2017, **12**, 132–136.

6 Y. Xie, T. Chen, Y. Guo, Y. Cheng, H. Qian and W. Yao, *Food Chem.*, 2019, **270**, 173–180.

7 Y. Guo, H. Wang, X. Ma, J. Jin, W. Ji, X. Wang, W. Song, B. Zhao and C. He, *ACS Appl. Mater. Interfaces*, 2017, **9**, 19074–19081.

8 H. Zhao, J. Jin, W. Tian, R. Li, Z. Yu, W. Song, Q. Cong, B. Zhao and Y. Ozaki, *J. Mater. Chem. A*, 2015, **3**, 4330–4337.

9 Y. Guo, Y. Tao, X. Ma, J. Jin, S. Wen, W. Ji, W. Song, B. Zhao and Y. Ozaki, *Chem. Eng. J.*, 2018, **350**, 120–130.

10 X. Ma, S. Wen, X. Xue, Y. Guo, J. Jin, W. Song and B. Zhao, *ACS Appl. Mater. Interfaces*, 2018, **10**, 25726–25736.

11 W. Song, C. J. Querebillo, R. Goetz, S. Katz, U. Kuhlmann, U. Gernert, I. M. Weidinger and P. Hildebrandt, *Nanoscale*, 2017, **9**, 8380–8387.

12 J. Jin, S. Zhu, Y. Song, H. Zhao, Z. Zhang, Y. Guo, J. Li, W. Song, B. Yang and B. Zhao, *ACS Appl. Mater. Interfaces*, 2016, **8**, 27956–27965.

13 L. Wei, C. Yu, Q. Zhang, H. Liu and Y. Wang, *J. Mater. Chem. A*, 2018, **6**, 22411–22436.

14 X. Hu, X. J. Hu, Q. Q. Peng, L. Zhou, X. F. Tan, L. H. Jiang, C. F. Tang, H. Wang, S. H. Liu, Y. Q. Wang and Z. Q. Ning, *Chem. Eng. J.*, 2020, **380**, 11.

15 M. R. Al-Mamun, S. Kader, M. S. Islam and M. Z. H. Khan, *J. Environ. Chem. Eng.*, 2019, **7**, 17.

16 L. G. Devi and R. Kavitha, *Appl. Surf. Sci.*, 2016, **360**, 601–622.

17 P. D. Cozzoli, R. Comparelli, E. Fanizza, M. L. Curri, A. Agostiano and D. Laub, *J. Am. Chem. Soc.*, 2004, **126**, 3868–3879.

18 W. Song, W. Ji, S. Vantasin, I. Tanabe, B. Zhao and Y. Ozaki, *J. Mater. Chem. A*, 2015, **3**, 13556–13562.

19 J. Zhang, X. Jin, P. I. Morales-Guzman, X. Yu, H. Liu, H. Zhang, L. Razzari and J. P. Claverie, *ACS Nano*, 2016, **10**, 4496–4503.

20 N. Nhat Truong, M. Altomare, J. Yoo and P. Schmuki, *Adv. Mater.*, 2015, **27**, 3208–3215.

21 R. Zhang, H. Wang, S. Tang, C. Liu, F. Dong, H. Yue and B. Liang, *ACS Catal.*, 2018, **8**, 9280–9286.

22 K. Lee, H. Yoon, C. Ahn, J. Park and S. Jeon, *Nanoscale*, 2019, **11**, 7025–7040.

23 C. Kutahya, P. Wang, S. Li, S. Liu, J. Li, Z. Chen and B. Strehmel, *Angew. Chem., Int. Ed.*, 2020, **59**, 3166–3171.

24 J. Bian, C. Huang, L. Wang, T. Hung, W. A. Daoud and R. Zhang, *ACS Appl. Mater. Interfaces*, 2014, **6**, 4883–4890.

25 X. Zhang, F. Wang, H. Huang, H. Li, X. Han, Y. Liu and Z. Kang, *Nanoscale*, 2013, **5**, 2274–2278.

26 Y. Zhao, Q. Zeng, T. Feng, C. Xia, C. Liu, F. Yang, K. Zhang and B. Yang, *Mater. Chem. Front.*, 2019, **3**, 2659–2667.

27 S. Sharma, V. Dutta, P. Singh, P. Raizada, A. Rahmani-Sani, A. Hosseini-Bandegharaei and V. K. Thakur, *J. Cleaner Prod.*, 2019, **228**, 755–769.

28 S. J. Zhu, Q. N. Meng, L. Wang, J. H. Zhang, Y. B. Song, H. Jin, K. Zhang, H. C. Sun, H. Y. Wang and B. Yang, *Angew. Chem., Int. Ed.*, 2013, **52**, 3953–3957.

29 W. Zhu, M. Li, S. Chen, C. Wang and X. Lu, *Appl. Surf. Sci.*, 2019, **491**, 138–146.

30 Y. Wan, Z. Guo, X. Jiang, K. Fang, X. Lu, Y. Zhang and N. Gu, *J. Colloid Interface Sci.*, 2013, **394**, 263–268.

31 J. Liu, D. Li, K. Zhang, M. Yang, H. Sun and B. Yang, *Small*, 2018, 1703919.

32 T. Feng, Q. Zeng, S. Lu, X. Yan, J. Liu, S. Tao, M. Yang and B. Yang, *ACS Photonics*, 2018, **5**, 502–510.

33 J. Liu, S. Lu, Q. Tang, K. Zhang, W. Yu, H. Sun and B. Yang, *Nanoscale*, 2017, **9**, 7135–7142.

34 W. Song, Y. F. Wang, H. L. Hu and B. Zhao, *J. Raman Spectrosc.*, 2007, **38**, 1320–1325.

35 W. D. Zhu, M. Q. Chi, M. Gao, C. Wang and X. F. Lu, *J. Colloid Interface Sci.*, 2018, **528**, 410–418.

36 H. Y. Zhao, Y. Guo, S. J. Zhu, Y. B. Song, J. Jin, W. Ji, W. Song, B. Zhao, B. Yang and Y. Ozaki, *Appl. Surf. Sci.*, 2017, **410**, 42–50.

37 A. D'Agostino, A. M. Giovannozzi, L. Mandrile, A. Sacco, A. MarioRossi and A. Taglietti, *Talanta*, 2020, **216**, 120936.

38 L. Zhou, J. Zhou, W. Lai, X. Yang, J. Meng, L. Su, C. Gu, T. Jiang, E. Y. B. Pun, L. Shao, L. Petti, X. W. Sun, Z. Jia, Q. Li, J. Han and P. Mormile, *Nat. Commun.*, 2020, **11**, 1785.

39 Z. Niu, C. Zhou, J. Wang, Y. Xu, C. Gu, T. Jiang, S. Zeng, Y. Zhang, D. S. Ang and J. Zhou, *J. Mater. Sci.*, 2020, **55**, 8868–8880.

40 Y. Tian, H. Liu, Y. Chen, C. Zhou, Y. Jiang, C. Gu, T. Jiang and J. Zhou, *Sens. Actuators, B*, 2019, **301**, 127142.

41 W. Song, Y. Wang and B. Zhao, *J. Phys. Chem. C*, 2007, **111**, 12786–12791.

42 X. Liang, B. L. Liang, Z. H. Pan, X. F. Lang, Y. G. Zhang, G. S. Wang, P. G. Yin and L. Guo, *Nanoscale*, 2015, **7**, 20188–20196.

43 X. Zhang, Z. Yu, W. Ji, H. Sui, Q. Gong, X. Wang and B. Zhao, *J. Phys. Chem. C*, 2015, **119**, 22439–22444.

44 W. Ji, B. Zhao and Y. Ozaki, *J. Raman Spectrosc.*, 2016, **47**, 51–58.

45 J. Y. Qin and H. P. Zeng, *Appl. Catal., B*, 2017, **209**, 161–173.

46 Y. Takahashi and T. Tatsuma, *Appl. Phys. Lett.*, 2011, **99**, 182110.

47 Z. Guan, P. Jin, Q. Liu, X. Wang, L. Chen, H. Xu, G. Song and R. Du, *J. Alloys Compd.*, 2019, **797**, 912–921.

48 H. Qian, Q. Hou, E. Duan, J. Niu, J. Nie, C. Bai, X. Bai and M. Ju, *J. Hazard. Mater.*, 2020, **391**, 122246.